

ROTOR-HEAD/FUSELAGE INTERACTIONAL EFFECTS ON HELICOPTER DRAG: INFLUENCE OF THE COMPLEXIFICATION OF THE ROTOR-HEAD GEOMETRY

D. Desvigne & D. Alfano
Eurocopter S.A.S.
Marseille-Provence International Airport
F-13725 Marignane cedex
France

Abstract

In this work supported by the European Clean Sky JTI Green Rotorcraft research programme, a step-by-step increasing complexity of the rotor-head geometry of a Eurocopter Dauphin AS365 N3 model is numerically investigated. It is aimed at discerning the rotor-head subcomponents responsible for strong interactions with the fuselage and how they contribute to airframe/flow interactions. Those interactions are usually at the origin of significant additional drag, and are consequently expected to be reduced within the framework of modern helicopter developments.

The computational strategy consists in adding to the rotor-head geometry a single rotor-head subcomponent for each iteration of the geometrical complexification process. Accordingly, a total of seven different configurations have been studied, from the isolated fuselage case to the most complex case of a fuselage-mounted rotor head involving mast, hub, beanie, blade sleeves, blade roots, non-rotating plate, swashplate, control rods, and scissors.

Both steady-state & unsteady RANS simulations have been performed using the ONERA's structured-mesh based finite-volume *elsA* solver to characterise rotor-head/fuselage interactions. Two different azimuthal locations of the rotor head have been considered for the steady-state computations, namely 0° and 45° with respect to freestream direction. Meshing has been created by resorting to overset structured grids. Bidirectional communications between overlapping grids are ensured by second-order Chimera interpolation techniques on the flow variables.

All the computations indicate that major direct drag contributors are the blade sleeves, rotor shaft (mast, hub and beanie) and blade roots. Indirect drag, defined as an increase of the fuselage drag due to interactions with wakes coming from the rotor head, is principally generated by the blade sleeves and blade roots. Locations of indirect drag generation over the fuselage are also addressed. Despite significant discrepancies in absolute drag levels, steady-state computations seem capable to capture each component's relative mean-drag contribution as compared to more demanding URANS simulations with acceptable fidelity.

1. MOTIVATIONS

The Clean Sky Joint Technology Initiative (JTI) is a European Research Programme aimed at greening Air Transport through the development of more environmentally-friendly advanced technologies. It is organised into six Integrated Technology Demonstrators (ITD) covering a large variety of themes: fixed-wing aircraft, rotorcraft, engines, systems, and eco-design concepts. Eurocopter is involved with other partners in the Green Rotorcraft (GRC) programme which is one of the Clean Sky ITDs. The GRC top objectives are a reduction of CO₂ emissions by 25 to 40%, together with a reduction of the perceived noise on ground by 10 EPNdB, and a full conformity with the European Union Regulation REACH protecting human health and environment from noxious chemical substances.

CO₂ emissions are function of fuel consumption, and consequently of the power required to fly, which directly depends on the design of the airframe and of the non-lifting rotating components for forward flight. Airframe and rotor-head components are main contributors to drag, so that a redesign has to be considered in order to fulfil expected objectives.

One of preliminary phases of the Clean Sky GRC programme consisted in a comprehensive drag analysis for three different helicopter weight-classes. It was focused on identifying components from which significant gains could be obtained, depending on the specific architecture of each weight class.

In this work, the drag assessment achieved for medium-weight helicopters is presented. The Dauphin AS365 N3 has been selected as reference. The analysis tackles direct drag, but also the indirect drag generated by the non-lifting rotating components, defined as the increase of the total fuselage drag — regarding the isolated fuselage case — due to interactions with wakes coming from the rotor head. This indirect drag may turn out to be significant, as it can represent up to 12% of the total helicopter drag in some situations [1].

Numerical tools have been preferred over wind-tunnel tests, for schedule-and-cost reasons. But it can also be argued that CFD solvers are mature enough to offer reliable drag estimations, as shown in [2,3]. In addition, wind-tunnel measurements of interaction drag or direct drag of some subcomponents remain difficult to perform.

Thus, in the following, drag evaluations rely exclusively on numerical computations.

2. COMPUTATIONAL PROCEDURE

Estimating numerically drag forces over bodies demands accurate simulations of the flow developing around them, which remains quite challenging for a fuselage-mounted rotor hub of a helicopter. The global flow is usually the result of numerous interactions between all the rotor-hub subcomponents [4]. Accordingly, investigating the aerodynamic characteristics of each rotor-head subcomponent separately may be irrelevant for a global understanding of rotor-head flows, because their isolated aerodynamic behaviour is severely altered when operating together with all other rotor-hub subcomponents and the fuselage. Another difficulty comes from the very complex geometry of the rotor head, exhibiting numerous details, sharp angles, and cavities.

2.1. Description of the numerical model and simplifications

The first step of this study consists in cleaning up the CAD of the fuselage, and in simplifying geometry of all the rotor-head subcomponents. This step is clearly motivated by the following observations:

- General trends in drag contributions are expected not to be significantly modified by local details of the geometry.
- Models for wind-tunnel tests are usually similarly simplified.
- Human cost required for the meshing activities is considerably reduced, compared to the situation of the generation of a structured mesh including all the geometrical details of the rotor hub.

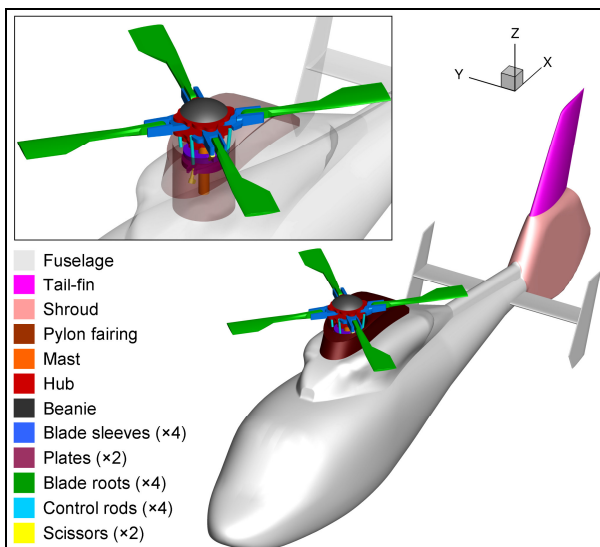


Figure 1: Overview of the simplified AS365 N3 numerical model, and definition of the 12 subcomponents

Thus, the choice was made to investigate a simplified fuselage of a Dauphin AS365 N3 at scale 1:7.7 for which air intakes, engine exhausts, and shroud have been filled up, as exhibited in Figure 1. The fuselage is equipped with a Starflex rotor-head instead of its original Spheriflex architecture. In addition, all the very small details of rotor-hub subcomponents have been smoothed. The blade-

root shape has been simplified as well. The rotor head appears in its simplified form as the assembly of floating parts.

During the drag analysis, it has been required to split the whole geometry into 12 elementary subcomponents (or families), as shown in Figure 1. The whole fuselage has been split into 4 families, namely tail-fin, shroud, pylon fairing and the rest of fuselage, corresponding to the cell, the engine cowlings, the rear ramp, the tail-boom and the empennage. The rotor head is made of 8 subcomponents: mast, hub, beanie, blade sleeves, blade roots, plates (gathering swashplate and non-rotating plate), control rods and scissors.

2.2. CFD solver and numerical features

The drag analysis activities have been organised into two phases. Within the frame of the first phase, drag evaluations have been obtained from 3-D steady Reynolds Averaged Navier-Stokes (RANS) CFD computations. Two different azimuthal locations of the rotor head have been selected — 0° and 45° with respect to the freestream direction as depicted in Figure 2 — in order to evaluate the influence of the rotor-head azimuthal location on drag estimations based on steady-state simulations.

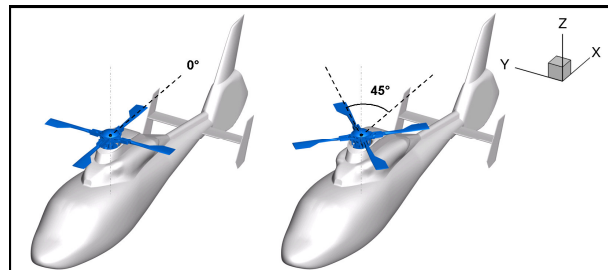


Figure 2: Overview of the two different azimuthal locations of the rotor head, for steady RANS computations

The second phase consisted in 3-D unsteady RANS (URANS) computations, and was focused on clarifying a certain number of recurring questions: namely the capability of steady-state simulations to retrieve drag breakdowns or airframe/flow interactional effects on drag obtained from more accurate unsteady computations, or the level of enhancement brought by unsteady simulations given the significant increase of required resources, on absolute drag levels for instance.

The structured-mesh based flow solver *e/sA* v3.3, developed by the French Aerospace Lab (ONERA) has been used. The spatial discretization is based on finite-volume techniques. A second-order centred Jameson scheme has been used, together with artificial dissipations of second and fourth orders for discontinuity capturing and spurious oscillation damping. Dissipation coefficients have been taken as $\chi_2 = 0.5$ and $\chi_4 = 0.016$ respectively.

For steady-state computations, a second order backward Euler integration with implicit LU scheme has been employed for pseudo-time advancement. The Courant-Friedrichs-Lewy (CFL) constant has been taken as a linear variation from 0.5 for the first 100 iterations to 10 after 3000 iterations. A total of 20000 iterations have been required to ensure an acceptable convergence of all

the RANS simulations presented in the following. For unsteady computations, a 30-substep Gear integration scheme has been employed. The strategy has consisted in performing eight rotor-head revolutions from an initialisation based on the steady-state situation. The azimuthal discretization $\Delta\Psi$ has been taken as 10° for the first three revolutions, then 5° for the next three revolutions and 2° for the last two revolutions. Drag analysis is based on averaging over the last revolution. A smaller azimuthal discretization has turned out to significantly increase computational costs, which were not affordable given the time dedicated to the study.

Fully turbulent flows have been assumed with the $k-\omega$ SST turbulence model of Menter [5].

2.3. Growing complexity of the rotor-head geometry and related run description

A fuselage without rotor head has first been simulated in order to obtain the reference direct drag level of the fuselage. Then rotor-head subcomponents have been added step by step in a geometrical complexification process, which enables the assessment of their contribution on the airframe/flow interaction drag. Consequently, a total of seven steady-state runs have been performed for the case of a rotor head located at azimuth 0° . All the subcomponents retained for each run are summarised in Table 1.

Subcomponent	Run number						
	#0	#1	#2	#3	#4	#5	#6
Fuselage	✓	✓	✓	✓	✓	✓	✓
Tail-fin	✓	✓	✓	✓	✓	✓	✓
Shroud	✓	✓	✓	✓	✓	✓	✓
Pylon fairing	✓	✓	✓	✓	✓	✓	✓
Mast	✗	✓	✓	✓	✓	✓	✓
Hub	✗	✓	✓	✓	✓	✓	✓
Beanie	✗	✓	✓	✓	✓	✓	✓
Blade sleeves	✗	✗	✓	✓	✓	✓	✓
Plates	✗	✗	✗	✓	✓	✓	✓
Blade roots	✗	✗	✗	✗	✓	✓	✓
Control rods	✗	✗	✗	✗	✗	✓	✓
Scissors	✗	✗	✗	✗	✗	✗	✓

Table 1: Subcomponents retained for each run

Run #0 corresponds to the case of an isolated fuselage. Runs #1 to #6 consist in increasing the rotor-hub complexity with the addition of more and more rotor-head subcomponents, together with the isolated fuselage. The complete rotor-hub is treated in run #6. Indirect drag is calculated as the difference between fuselage drag obtained for the considered run and the reference drag of the isolated fuselage estimated from run #0. Accordingly, runs #1 to #6 make it possible to estimate the increase of interaction drag with an increase of geometrical complexity of the rotor hub. Only run #6 has been performed for the case of a rotor head located at 45° and only runs #0 and #4 have been achieved by URANS computations.

2.4. Chimera strategy

The *Chimera* technique has been first introduced by Benek et al. [6,7]. It consists in meshing a complex

geometry by overlapping elementary grids that bidirectionally communicate by interpolations. This approach is particularly adapted when the geometry is made of independent subcomponents, or when some subcomponents are in motion. In addition, it makes it possible to add new subcomponents to an existing assembly just by grid superpositions, without remeshing all the geometry. Accordingly, Chimera interpolation techniques seem quite appropriate for computing flows developing over different fuselage-mounted rotor hubs.

2.4.1. Grid description

All the components have been meshed with multi-block based structured grids, as well as background grids in which the helicopter-component grids are immersed. The grids have been created using the commercial structured grid generator Ansys ICEM CFD and Airbus' in-house mesh generators. The main features describing each elementary grid are summarised in Table 2. Figure 3 and Figure 4 offer an overview of the fuselage (FUS) and rotor-hub background (BKT) meshes respectively. A magnified view of the rotor-head skin mesh for run #6 is depicted in Figure 5. The total number of points, topological blocks & CPUs required for each run are reported in Table 3.

The number of CPUs required for each simulation has been chosen to maintain a global load beyond 350 000 points per CPU. An amount of roughly 100 million points — distributed over 348 CPUs — were needed for the most demanding run (run #6).

Elementary grid	Code	Nr of blocks	Nr of pts ($\times 10^6$)
Overall Background	BCK	24	5.63
Rotor-hub Background	RHB	352	28.36
Rear-part Background	RPB	22	5.71
Total fuselage (fuselage, tail-fin, shroud, pylon fairing)	FUS	205	20.26
Shaft (mast, hub, beanie)	SHF	171	14.10
Blade sleeves	BS	284	11.40
Non-rotating plate	NRP	21	1.89
Swashplate	SWP	24	1.28
Blade roots	BR	412	8.08
Control rods	CR	16	0.64
Scissors	SC	33	0.71

Table 2: Number of topological blocks & points

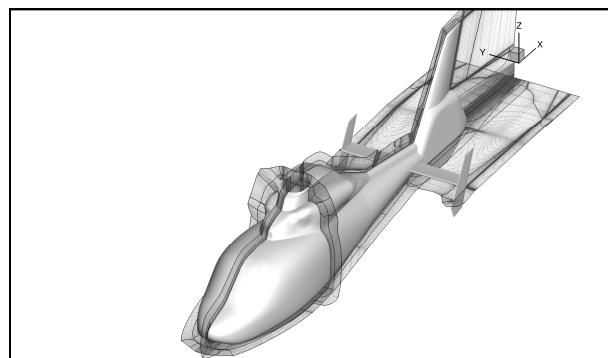


Figure 3: Overview of the fuselage mesh

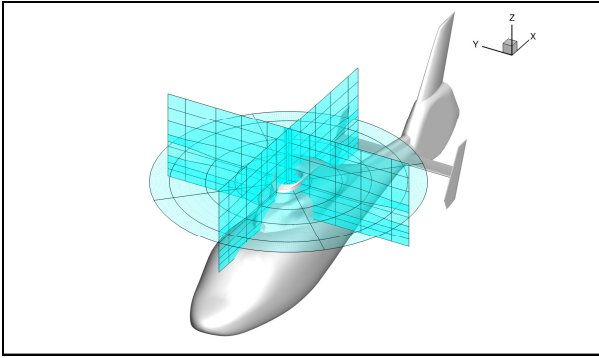


Figure 4: Overview of the rotor-hub background mesh

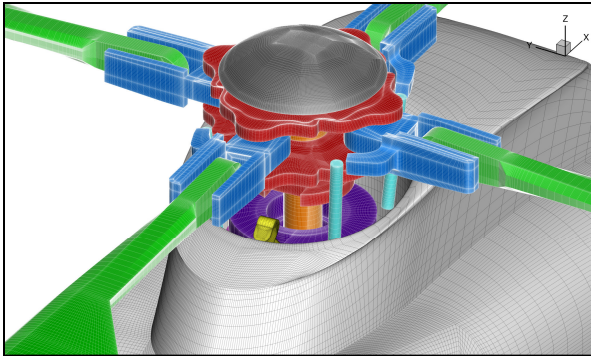


Figure 5: Skin mesh of the rotor-hub & fuselage for run #6

Run number	Nr of block	Nr of pts ($\times 10^5$)	Nr of CPUs	Global load ($\times 10^6$)
#0	229	25.89	96	0.27
#1	774	74.06	228	0.33
#2	1058	85.46	264	0.32
#3	1103	88.63	312	0.28
#4	1515	96.71	348	0.27
#5	1531	97.35	348	0.28
#6	1564	98.07	348	0.28

Table 3: Total number of topological blocks, points ($\times 10^6$), CPUs & global load (points per CPU, $\times 10^6$) for each run

First points normal to walls have been set to ensure a dimensionless wall distance between 0.1 and 3 to all walls.

2.4.2. Chimera interpolations

When assembled, each grid has boundaries — *fringe points* — which lie in the interior of a neighbouring grid, and require information from that containing grid. Boundary information is exchanged between the grids via interpolations or extrapolations of the flow variables. In what follows, a second-order explicit interpolation scheme based on Lagrange polynomials has been chosen to ensure an acceptable accuracy in overlap zones [8]. Interpolations degenerate into extrapolations when receiver points are not included in donor-point stencils.

Extrapolated receiver points are considered as critical — *orphan* — points, if no donor points ensuring satisfying extrapolations can be found by the donor-point search algorithm. The presence of orphan points is frequent if the two grids exhibit severe spatial-discretization discrepancies in the communication zone. This is

particularly true for communication zones located in the vicinity of walls, where the donor grid exhibits highly refined cells for accurate estimations of velocity gradients at the wall, while the receiver grid is made of large cells, when acting as a background mesh for example. An Alternative Digital Tree (ADT) preconditioning-based technique with *e/sA* default parameters has been used to determine donor cells. More details about the ADT preconditioning are available in [9].

Grid points superposing a non-fluid area also have to be blanked. The overlap zones have been built to be as small as possible in order to limit redundant point regions where solution is computed twice. Yet, for the sake of consistency, the overlap zones must be wide enough to prevent from donor points of one communication being receiver points of the reciprocal communication, as shown in Figure 6, which would imply implicit interpolations.

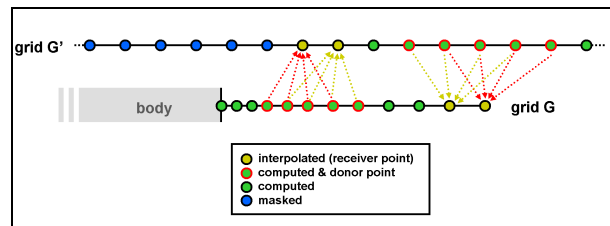


Figure 6: 1-D view of bidirectional communications in an overlap zone (example of a two-point layer of receiver points, each requiring four donor points)

2.4.3. Two-level Chimera assembly

To prevent from the creation of orphan points, and because of the complexity of the rotor-hub geometry, the choice was made to construct a two-level Chimera assembly. It consists in designing a background grid (RHB) of intermediate mesh-size, which is dedicated to communications at rotor-hub local level. Thus, each rotor-hub subcomponent body is blanked into that grid while communicating with it by interpolations. The RHB grid is then partially masked into the overall background grid (BCK), while ensuring at the same time communications at global level between rotor head and the overall background grid. A schematic view of the two-level Chimera assembly is presented in Figure 7.

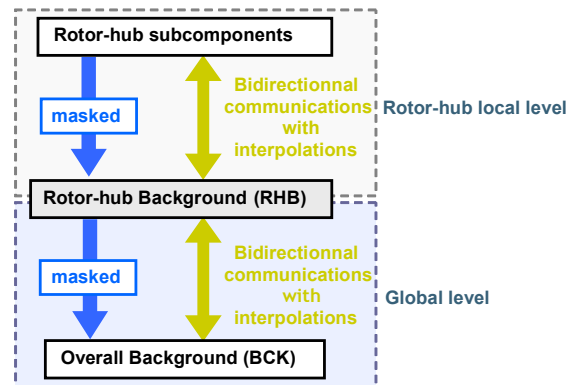


Figure 7: Schematic view of the two-level Chimera assembly

This technique prevents from masking each rotor-hub subcomponent directly into the rough BCK grid, which

would result in a massive orphan-generating assembly because of severe mesh-size discrepancies between all the grids in the communication zones.

Masking has been achieved by the Meakin X-ray technique [10].

To further illustrate how the two-level Chimera assembly is achieved, node/point functions of the overall background grid (BCK) are highlighted in Figure 8. These functions correspond to global-level communications where information is transferred from the total fuselage grid (FUS) and the rotor-hub background (RHB) at the two layers of interpolated points.

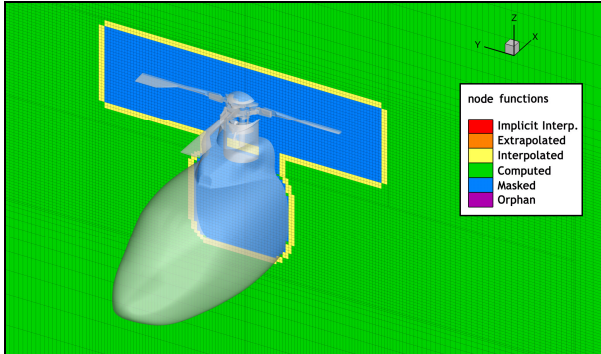


Figure 8: Overall background node functions for run #6

Rotor-hub local-level Chimera communications are illustrated by Figure 9, which shows how each rotor-hub subcomponent is blanked into the rotor-head background grid (RHB), and where the RHB grid receives data from all the local subcomponent surrounding grids.

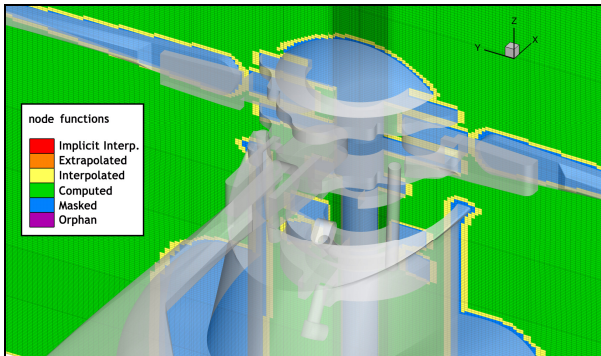


Figure 9: Rotor-hub background node functions for run #6

For the sake of consistency, each subcomponent crossing another subcomponent grid has to be blanked and interpolated at the subcomponent level as well, as depicted in Figure 10, which can lead to numerous interactions between all the subcomponents grids.

2.5. Flight conditions

Flight conditions used for all the runs are reported in Table 4. Pitch angle was obtained from a previous HOST computation for the corresponding flight conditions. The HOST code is a Eurocopter in-house simulation tool which provides helicopter & rotor trims [11]. No blade pitch, lag and flap have been taken into account regarding the azimuthal locations of the four blade sleeves and roots.

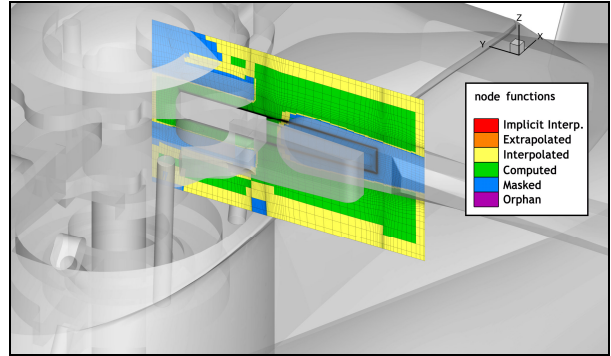


Figure 10: Blade-sleeve #2 grid node functions for run #6

Variables	Value
Pressure (p_∞):	101320 Pa
Temperature (T_∞):	288 K
Air density (ρ_∞):	1.225 kg/m ³
Incoming flow velocity (U_∞):	70 m/s
Pitch angle (α , positive up):	-5.3°
Sideslip angle (β):	0°
Rotor rotational speed (N_r):	1315 RPM (URANS only)
Incoming-flow direction:	e_x

Table 4: Flight-condition characteristics

3. NUMERICAL RESULTS

3.1. Steady RANS computations

3.1.1. Convergence

Figure 11 shows the variations of the residual of density regarding iterations for the complete configuration (run #6) with a rotor-head azimuth of 0°. A loss of 4 orders of magnitude of the residual is highlighted within a first period of 10000 iterations, hence demonstrating an acceptable convergence level of the RANS computations.

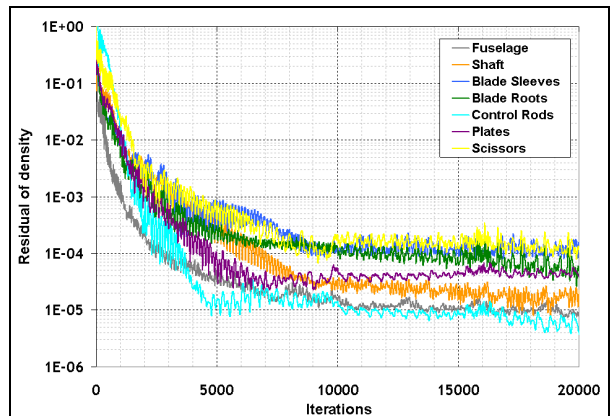


Figure 11: Residual-of-density history; rotor head at 0°, run #6

Dimensionless drag-surface variations with iterations are exhibited in Figure 12 for the same run. Almost constant drag contributions are obtained for every subcomponent after 10000 iterations. It confirms the fair convergence of the simulations. Nevertheless, fuselage reveals some small oscillations in the “converged” region. This is

because flow separations at aft cowlings, rear ramp and tail parts entail a natural pressure unsteadiness in their vicinity.

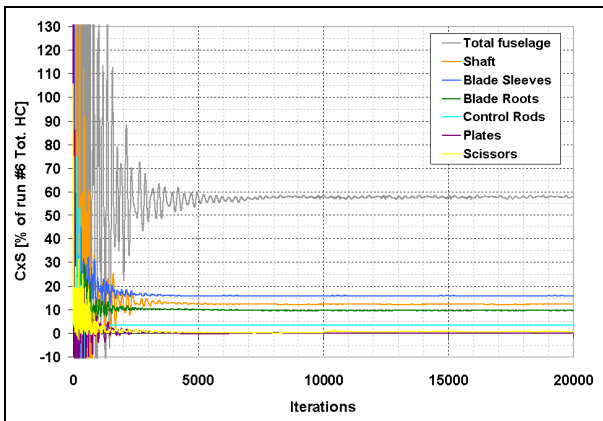


Figure 12: Dimensionless drag-surface history; rotor head at 0°, run #6

3.1.2. Drag breakdown for the complete configuration

In this section, only the configuration of a rotor head azimuthally located at 0° is presented. Drag levels have been evaluated by averaging computed drag surfaces CxS over the last period of 5000 iterations, in order to smooth the influence of spurious oscillations, as previously illustrated in Figure 12.

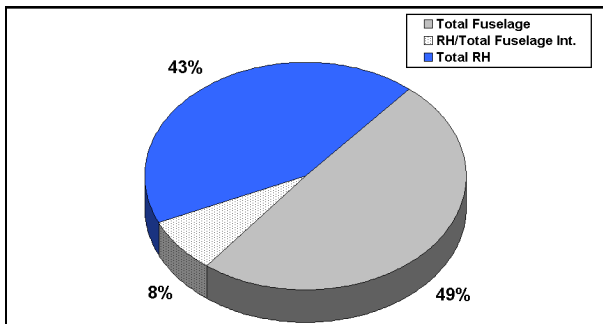


Figure 13: Global drag breakdown; rotor head at 0°, run #6

Figure 13 shows the global drag breakdown obtained for the complete configuration (run #6). The rotor-head/total fuselage interaction drag has been estimated as the difference between the drag of the total fuselage and the drag of the isolated total fuselage obtained from run #0. It reveals that the rotor head (RH) is directly responsible for 43% of the total helicopter drag. Its indirect contributions through wake/fuselage interactions represent up to 8% of the total drag.

A comprehensive drag breakdown computed from run #6 results is exposed in Figure 14. For fuselage, tail-fin, shroud and pylon fairing, direct drag is exhibited, as well as indirect drag (in dotted bars) corresponding to their additional amount of drag due to interactions with the rotor head. For the non-lifting rotating components — blade sleeves, blade roots, shaft, control rods, swashplate and scissors — it has been hypothesized that their interactions with the other rotor-head subcomponents remain small, so that corresponding drag levels reported in Figure 14 represent direct contributions

only. This will be reconsidered for blade sleeves in section 3.1.3.

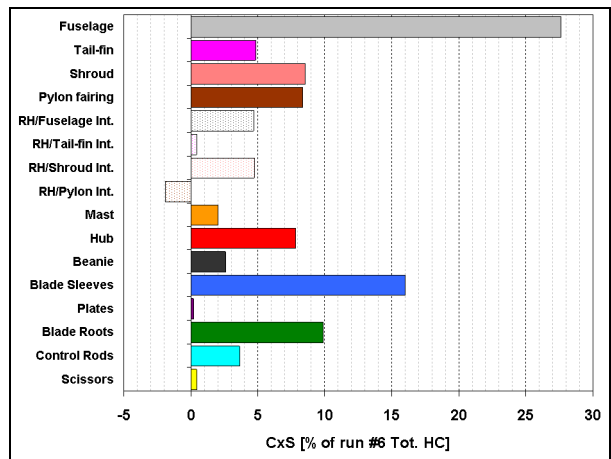


Figure 14: Detailed drag breakdown; rotor head at 0°, run #6

Figure 14 shows that the main contributors for direct rotor-head drag are the blade sleeves — for 16% of the total helicopter drag — then the blade roots (10%) and the hub (8%). The scissors and the plates (non-rotating plate and swashplate) are negligible sources of drag (0.5% and 0.2% respectively), probably because they are shielded by the pylon fairing, and almost completely included in the cavity of the rotor head.

Indirect drag contributions reach up to 8% of the total helicopter drag, which is equivalent to the direct-drag level of the hub, shroud or pylon fairing. The presence of the rotor head entails an increase of drag of the fuselage and shroud by roughly 5% of the total helicopter drag. It has almost no influence on tail-fin drag (0.5%). For pylon fairing, a decrease by 2% is observed. Some explanations of this negative contribution to interactional drag are suggested in sections 3.1.7. and 3.1.8.

3.1.3. Analysis of interactional drag

In order to assess which rotor-head subcomponents contribute most to the generation of airframe/wake interaction drag — i.e. indirect drag — a comprehensive drag breakdown has been computed for each run, as exhibited in Figure 15 in terms of percentage of the complete rotor-head drag obtained from run #6.

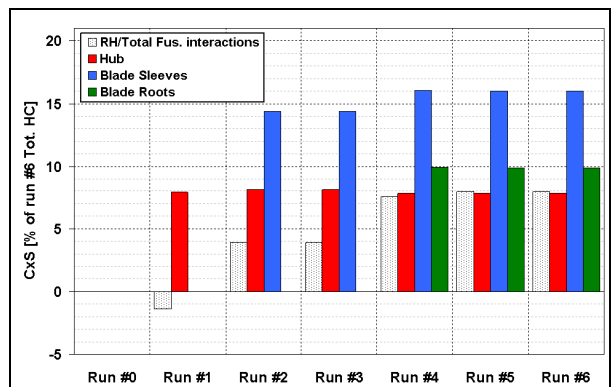


Figure 15: Variations of drag of major contributors with the rotor-head geometrical complexification; rotor head at 0°

It makes it possible to follow the variations of drag levels within the rotor-head geometrical complexification process. Two important rotor/fuselage interaction drag increases are observed between runs #1 and #2, and between runs #3 and #4, which correspond respectively to the addition of the blade sleeves and the blade roots (see Table 1). Blade sleeves, blade roots and control rods are responsible for 67%, 47%, and 4% of the total indirect drag respectively. The shaft (mast, hub and beanie) alone has a negative contribution to indirect drag by 17%.

The variations of drag of major contributors, namely the hub, blade sleeves and blade roots are also represented as a function of the runs. They exhibit rather small variations with the growing complexity of the rotor-head geometry, hence corroborating the previous hypothesis of limited interactions between all the rotor-head subcomponents. The only exception is for blade-sleeve related drag between runs #3 and #4: drag increases by 1.7% of the total helicopter drag, due to the addition of the blade roots, which indicates the presence of sleeve/root interactions at their junction. The addition of the non-rotating plate, swashplate, control rods and/or scissors has almost no effect on other component drag. Therefore the interactions between rotor-hub sub-components seem to be roughly limited to sleeve/root interactions.

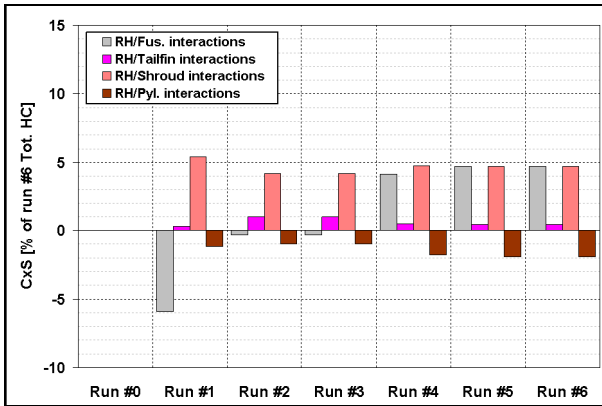


Figure 16: Variations of indirect drag with the rotor-head geometrical complexification; rotor head at 0°

Figure 16 shows a detailed view of the indirect-drag variations over different fuselage subcomponents as a function of the rotor-head growing complexity. The tail-fin and shroud exhibit a roughly constant increase of drag — by 5% and 0.5% of the total helicopter drag respectively — within the complexification process. Consequently, this indirect drag seems to be the results of interactions with shaft wake only.

Whatever the rotor-head complexity, pylon fairing shows negative indirect-drag generation. Shaft and blade roots seem to be the main contributors to this negative indirect drag.

Fuselage drag severely decreases with the addition of the shaft. This is probably due to the flow deflexion entailed by the beanie in the vicinity of aft engine cowlings. Important increases of indirect drag over the fuselage are then observed with the addition of the blade sleeves and blade roots, respectively by 5.6% and 4.5% of total

helicopter drag. Control rods are responsible for an increase of indirect drag over the fuselage by 0.6%.

Major results are summarised in Table 5.

Rotor-head subcomponent	Direct drag	Indirect drag (interactions)	
Blade sleeves	14.7%	5.6%	w/ fuselage -1.3%
Shaft (mast, hub, beanie)	12.5%	-5.9%	w/ fuselage 5.4% -1.2%
Blade roots	9.9%	4.5%	w/ fuselage 0.6% -0.8%
Control Rods	3.7%	0.6%	w/ fuselage 1.7%

Table 5: Direct-and-indirect drags of major contributors (% of total helicopter drag)

3.1.4. Pressure-related skin analysis

Drag created by the fluid over the complete helicopter is the combination of two types of drag: pressure drag (or form drag) and friction drag.

Pressure-drag force F_{PD} is the result of the pressure exerted by the fluid all over the structure. It may be investigated through a dimensionless pressure-drag coefficient C_{PD} which is locally evaluated from the skin pressure coefficient C_p and the local unit outward-pointing vector normal to the wall \mathbf{n} as:

$$(1) \quad C_{PD} = C_p (-\mathbf{n} \cdot \mathbf{e}_x)$$

In equation (1), the minus sign comes from conventions chosen in this work for the 3D orientation axes.

For low-speed flows, pressure coefficient C_p is expressed as:

$$(2) \quad C_p = \frac{p - p_\infty}{1/2 \rho_\infty U_\infty^2}$$

where p is the skin-pressure distribution resulting from the computation.

The distribution of pressure coefficient C_p over the complete helicopter skin is depicted in Figure 17 (run #6), for the azimuth 0°. Unsurprisingly, highest values of pressure coefficient are reached at the nose, cockpit and all the other frontal surfaces, such as the frontal main gear-box air intake, front pylon fairing, blade sleeves, front shroud and tail-fin leading edge. An interesting point to be underlined is the negative pressure coefficient at the rear engine cowlings and aft pylon fairing. The suction effect it entails may potentially result in significant drag generation, as investigated later on.

3.1.5. Friction-related skin analysis

Fiction-drag force F_{FD} arises from the friction of the fluid against the skin of the structure. It directly depends on the viscous-stress tensor at the wall $\tau_{|wall}$. Friction drag may be evaluated through a dimensionless friction-drag coefficient C_{SFD} which is locally estimated as:

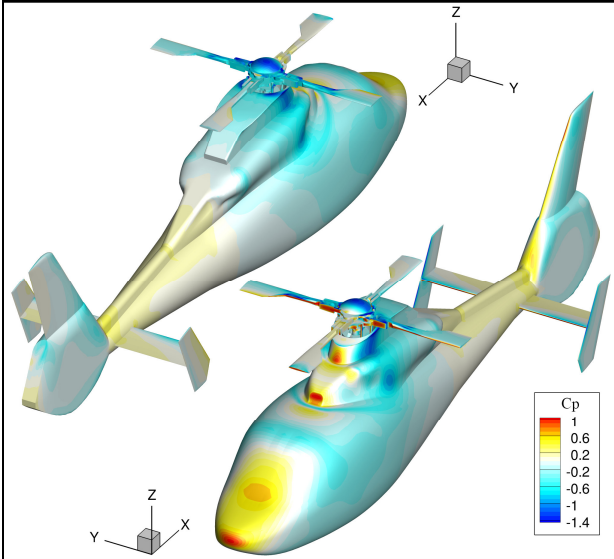


Figure 17: Skin distribution of pressure coefficient C_p

$$(3) \quad C_{SFD} = \frac{F_{sk_x}}{1/2 \rho_\infty U_\infty^2}$$

where F_{sk_x} is the streamwise component (x) of the local friction vector at skin \mathbf{Fsk} defined as:

$$(4) \quad \mathbf{Fsk} = \boldsymbol{\tau}_{|wall} \cdot \mathbf{n} - ((\boldsymbol{\tau}_{|wall} \cdot \mathbf{n}) \cdot \mathbf{n}) \mathbf{n}$$

which corresponds to the projection onto the local tangent plane at the wall of the viscous forces.

Skin frictions may be exhibited by resorting to skin-friction lines, which are lines tangent at each of their points to the skin friction vector \mathbf{Fsk} , as shown in Figure 18. The computation of skin-friction lines provides crucial information for the investigation of flow separations over the structure. Attached-flow regions correspond to zones where skin-friction lines point to the opposite direction of the helicopter motion, as shown by positive values of friction drag coefficient in Figure 18. Detached-flow and back-flow regions are located where skin-friction lines point to the direction of the helicopter motion, as represented by negative values of friction drag coefficient in Figure 18. Wide flow separations are highlighted at the rear parts of pylon fairing and at the aft engine cowlings. Massive detached-flow regions are also observed in the vicinity of blade sleeves.

3.1.6. Total-drag local coefficient

A total-drag local coefficient C_{TD} is constructed from pressure-drag and friction-drag coefficients as:

$$(5) \quad C_{TD} = C_{PD} + C_{SFD}$$

Total-drag surface $C_x S$ of each subcomponent is retrieved from integrating the total-drag local coefficient C_{TD} all over its surface S :

$$(6) \quad C_x S = \iint_S C_{TD} d\sigma$$

In the same way, total pressure-drag and friction-drag surfaces ($C_x S_{PD}$ and $C_x S_{SFD}$) may be estimated by

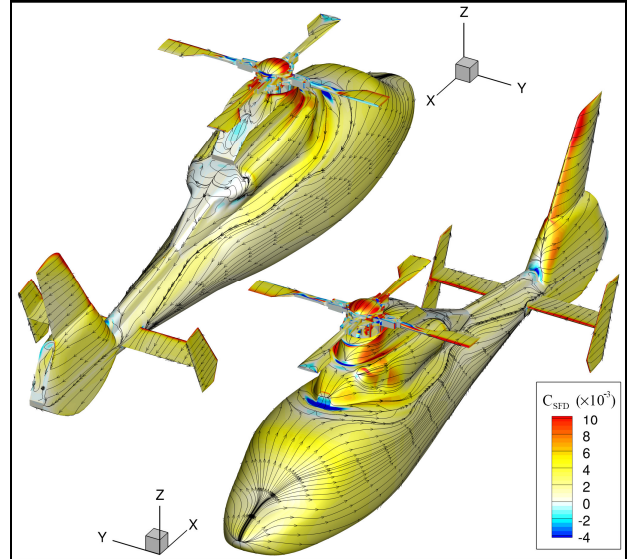


Figure 18: Skin distribution of friction-drag coefficient C_{SFD} , bounded between -0.004 and 0.01, and friction lines

replacing C_{TD} by C_{PD} and C_{SFD} respectively in the integrand in equation (6).

Accordingly, it is possible to assess where fuselage drag is locally generated from an evaluation of the distribution of the total-drag coefficient C_{TD} over the complete fuselage skin, as it appears in Figure 19, as well as the type of drag being generated, regarding the ratio $C_x S_{SFD} / C_x S_{PD}$.

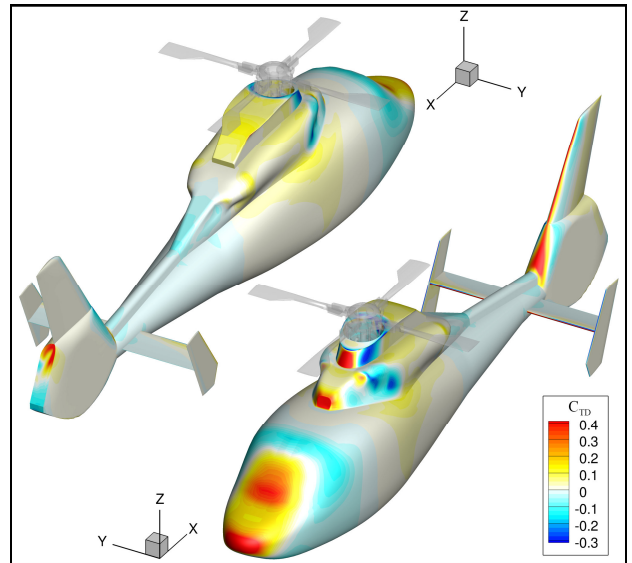


Figure 19: Whole-fuselage skin distribution of total drag coefficient C_{TD} , bounded between -0.3 and 0.4

It reveals that the complete fuselage drag is essentially generated at its front surfaces as expected, but also at the pylon fairing and engine cowlings, where a wide region of moderate C_{TD} is observed, despite a small streamwise component of the local unit vector normal to the wall in this zone. This drag generation comes from the presence of intense recirculations and massive separated flows, at the origin of a suction effect offering significant motion resistance. Integrated values of C_{SFD}

and C_{PD} over the total-fuselage skin indicate that friction drag represents up to 35% of the whole-fuselage drag.

3.1.7. Indirect-drag related fuselage skin analysis

A global localization of the generation of indirect drag has been estimated in Figure 14. It can be studied more locally by considering the difference of total-drag local coefficient obtained for the fuselage with the complete rotor head located at 0° (run #6) and for the isolated fuselage (run #0), respectively $C_{TD}^{\#6(0^\circ)}$ and $C_{TD}^{\#0}$:

$$(7) \quad \Delta_{TD\#0}^{\#6(0^\circ)} = C_{TD}^{\#6(0^\circ)} - C_{TD}^{\#0}$$

Figure 20 presents a view of the fuselage-skin distribution of this drag-coefficient difference. It indicates that indirect drag is generated on the fuselage at two locations: at the cowl frontal surface, due to flow modifications from the presence of the front blade, and at aft cowlings due to a possible impingement of wakes coming from the rotor head and deviated downwards by the beanie-induced deflection. A wide zone of negative difference is observable at aft pylon fairing. This negative interaction drag is likely the result of a masking effect from the aft blade which prevents the pylon fairing from being entirely impinged by the deflected flow. Indirect drag over the shroud is mostly generated at the junction with tail-boom and at rear surface where flow separations occur.

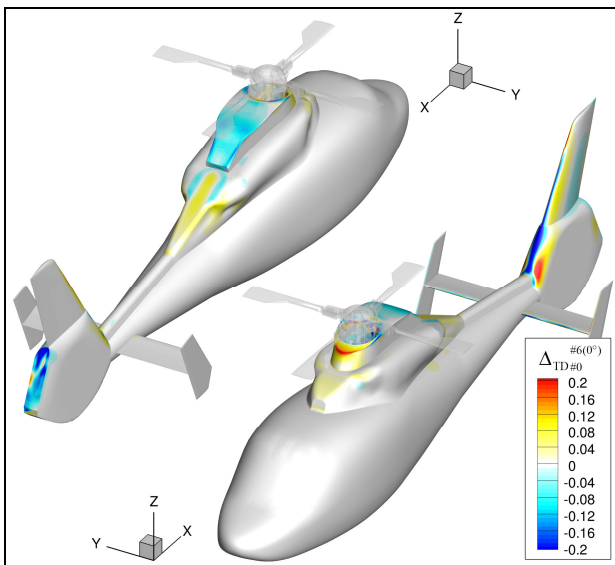


Figure 20: Skin distribution of difference of total-drag Δ_{TD} between the complete configuration with the rotor head at 0° (#6(0°)) and the isolated fuselage case (#0)

3.1.8. Wake overview

Only full 3-D unsteady CFD simulations with a rotating rotor head may obviously provide reliable data concerning wakes. However some rough information about wakes may be obtained from a volume-data analysis of less demanding steady-state simulations.

Figure 21 provides a qualitative overview of the wake by resorting to ribbon-based visualizations, for the isolated fuselage case (run #0) and the complete configuration (run #6). In both cases, blue ribbons reveal attached flow at the flat top-surface of the pylon fairing, whereas red

ribbons show impingement at aft engine cowlings. Blue ribbons also reveal a massive flow separation at the back surface of pylon fairing for the complete configuration. This separation appears not to be as wide for the isolated fuselage, for which blue ribbons remain downstream in the vicinity of the fuselage. Yellow ribbons point out flow separations at engine exhausts. In addition, all those ribbons impinge rear parts at the tail-fin and upper-shroud for the complete configuration, which is not the case for the isolated fuselage, for which they seem to be mostly located at mid-shroud and its junction with tail-boom.

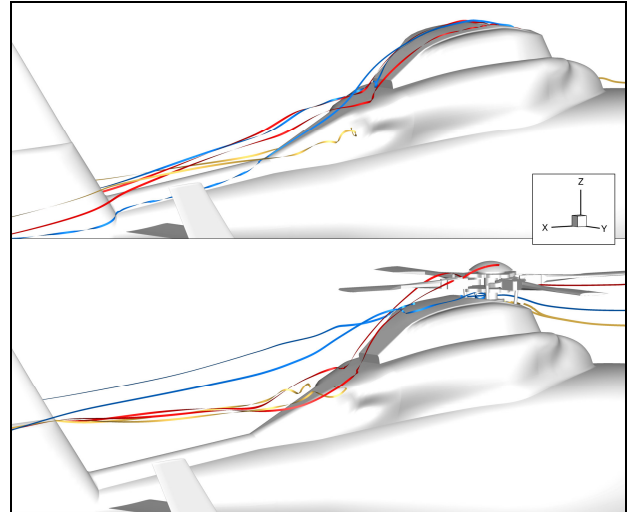


Figure 21: Wake overview with ribbons

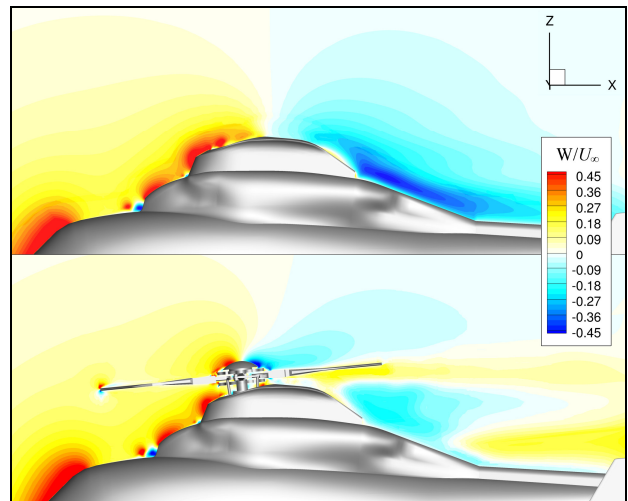


Figure 22: Dimensionless vertical-velocity field W/U_∞ in the $y = 0$ plane, bounded between -45% and 45%

To further illustrate why negative indirect drag is generated at the pylon fairing from a masking effect from the aft blade despite wider flow separations, vertical component W of the velocity field is investigated, as depicted in Figure 22. It indicates that the presence of the aft blade entails a significant loss of vertical velocity in the vicinity of the aft pylon fairing and rear engine cowlings. This loss of velocity comes together for low subsonic flows with a higher static pressure in those zones, resulting in a less intense pressure drop at aft pylon fairing and cowlings.

3.1.9. Influence of the rotor-head azimuth (RANS)

This subsection is focused on an evaluation of the influence of the rotor-head azimuth on drag breakdown.

RANS computations reveal that placing the rotor head from 0° to 45° entails a global reduction of drag by 5% of the total drag obtained for the complete configuration with a rotor head located at 0°. The drag breakdown obtained for the configuration with a 45°-located rotor head is shown in Figure 23 and compared to the 0° case. Each contribution is expressed as a percentage of total helicopter drag.

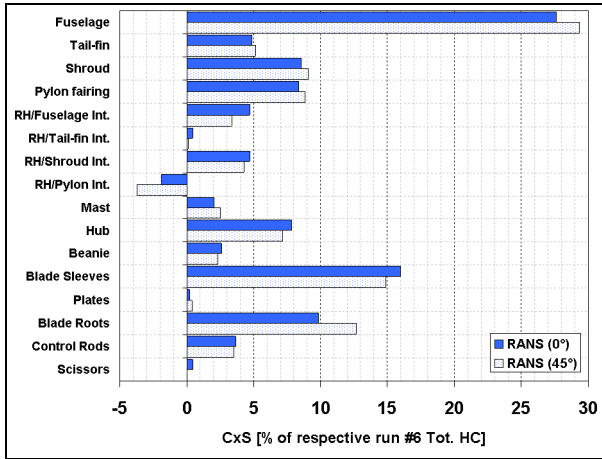


Figure 23: Comprehensive drag-breakdown for complete fuselage-mounted rotor head located at 0° and 45°, run #6

The drag contribution of all the items appear to be only slightly affected by a displacement of the rotor head from azimuth 0° to 45°, except for blade roots and rotor-head/pylon-fairing interactions. Blade-root contribution increases by 2.9%, reaching 12.7% of the whole helicopter drag. Rotor-head/pylon-fairing interactions are revealed to be much more drag-destructive by 1.9%, representing -3.7% of the whole helicopter drag. Other interaction drag-contributions have also been reduced. Total indirect drag due to interactions represents 4.1% of the total helicopter drag, instead of 8.0% obtained for the configuration with a 0°-located rotor head.

A view of the fuselage-skin distribution of the difference of total-drag densities obtained for the fuselage with the complete rotor head located at 45° and 0° highlights what has locally changed in the generation of indirect drag between the two configurations, as it appears in Figure 24. This total-drag coefficient difference is defined as:

$$(8) \quad \Delta_{TD}^{\#6(45^\circ)} = C_{TD}^{\#6(45^\circ)} - C_{TD}^{\#6(0^\circ)}$$

Figure 24 reveals that the decrease of rotor-head/pylon-fairing interaction drag observed in Figure 23 is mostly due to a significant decrease of drag coefficient at the pylon-fairing lateral walls entailed by the presence of blade sleeves and blade roots in their vicinity. Frontal engine cowlings and air intakes are also affected, as a drag-coefficient drop by 0.04 is observed, resulting in a smaller rotor-head/fuselage interaction drag. The back surface of the pylon fairing shows locally an increase of drag because it is no more masked by the aft blade.

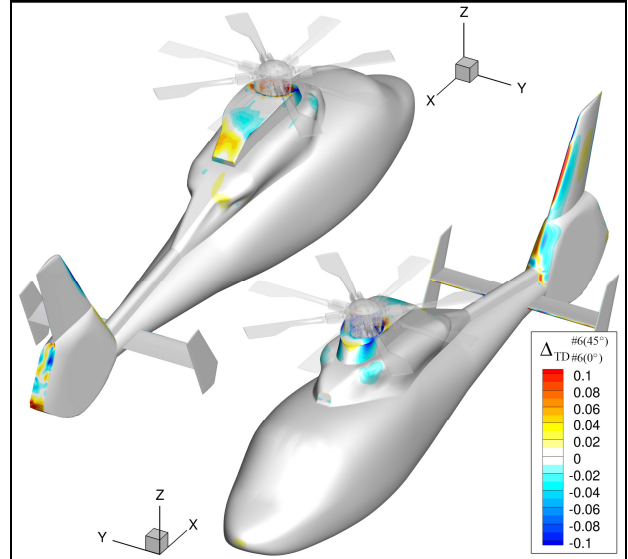


Figure 24: Skin distribution of total-drag coefficient difference Δ_{TD} between the complete configuration with the rotor head at 45° (#6(45°)) and 0° (#6(0°))

3.2. Unsteady RANS computations

This section aims to provide drag results obtained from unsteady RANS computations. Rotor clock-wise revolutions have been ensured by rotating all the moving rotor-head subcomponent grids, as well as the rotor-head background grid at each time step. A complete recalculation of receiver-and donor points, together with interpolation coefficients, has been required at each time step in order to achieve the simulations. Blades are azimuthally localized by the angle of blade #1 with the streamwise direction, noted ψ , as depicted in Figure 25.

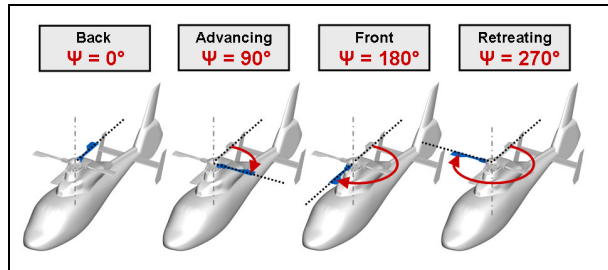


Figure 25: Specific positions of blade #1 and corresponding azimuth ψ

Numerical convergence has been ensured by a decrease of residual of density of one order of magnitude during Gear sub-iterations, together with a decrease of one order of magnitude from reducing the azimuthal step from 10° to 2°. Pseudo-periodic drag signals are observed after half a rotor revolution at $\Delta\psi = 2^\circ$.

3.2.1. Mean drag breakdown

Mean drag breakdown has been obtained from averaging unsteady drag levels of each item over the last revolution. It must be mentioned that an increase of the total helicopter drag by 19.9% has been observed from URANS run #4, compared with steady-state based computations with a rotor head maintained at azimuth 0°, but the drag global distribution shows only slight

discrepancies with what was obtained from RANS simulations, as exhibited in Figure 26. This increase of drag has revealed to be similar to the increase of drag observed by Borie *et al.* when confronting drag results obtained from RANS computations to measurements from wind-tunnel tests with a rotating rotor [1]. The rotor-head direct drag represents 41% of the total helicopter drag, while its indirect contribution through wake interactions with fuselage is roughly 6%.

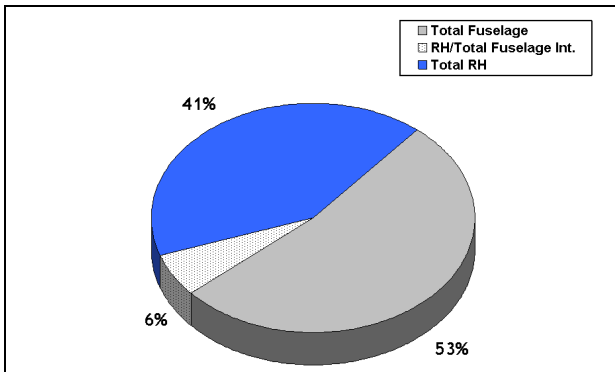


Figure 26: Global mean drag breakdown; URANS, run #4

A comprehensive mean-drag breakdown is presented in Figure 27, and compared to the one obtained from RANS simulations (run #4). Interaction mean-drag levels over different parts have been computed as the difference of mean drag levels obtained from run #4 and from the isolated fuselage case (run #0).

As for steady-state simulations, it appears that rotor-head direct mean-drag generation is dominated by the contributions of the blade sleeves, blade roots and the hub. The other item drag contributions are revealed to fairly agree for both computations, except for pylon fairing and mast, for which underestimations by 4.6% and 2.6% respectively are observed for the steady-state computation. In addition, indirect drag generated over fuselage, tail-fin, shroud and pylon appears to be overestimated by 1% to 2% in the RANS simulation.

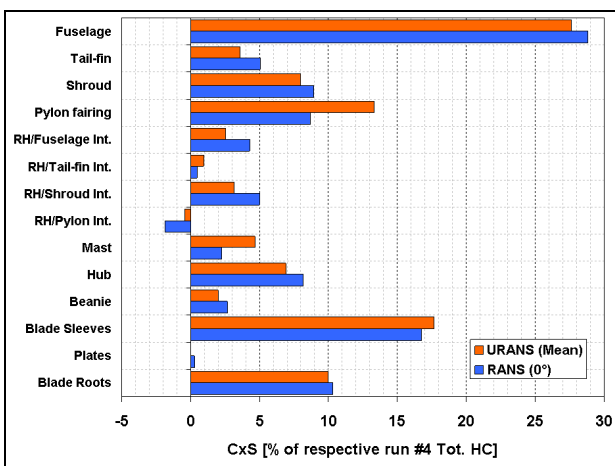


Figure 27: Comprehensive mean-drag breakdown comparison for URANS and RANS (0°); run #4

Despite discrepancies in absolute drag levels, the study reveals that steady-state computations seem rather capable to retrieve each subcomponent's relative mean-drag contribution obtained from more accurate — but

more demanding — URANS simulations with acceptable fidelity.

3.2.2. Unsteady drag

Unsteady drag signals presented in what follows are instantaneous signals obtained from the last revolution. Mean effects could be emphasized by a post-processing based on phase averaging over a greater number of revolutions. But this would require consequently the simulation of additional revolutions, which entails considerable computation time.

3.2.2.1. Rotating parts

Cumulated unsteady drag of the four blade sleeves is presented in Figure 28 over the last rotor revolution. The unsteady drag is clearly dominated by a 4Ω -component, Ω being the rotor frequency.

Maxima of drag are obtained for azimuths 0° , 90° , 180° and 270° . Those angles correspond to the situation of a rotor head with two of its four sleeves perpendicularly exposed to the incoming flow. A fraction of drag is pressure drag generated by the frontal flat surface of the advancing blade, while another fraction is pressure drag from the rear flat surface of the retreating sleeve. Those two fractions are quite similar because the difference of incoming flow velocity due to rotation remains small, roughly 10 m/s for the investigated flight conditions (see Table 4). In addition, a limited fraction of drag comes from sleeve-sleeve interactions, as well as interactions with other rotor-head subcomponents such as blade roots. Minima of drag are observed when the rotor head is azimuthal located at roughly 60° , 150° , 240° and 330° . A Fourier analysis also demonstrates the presence of 8Ω - and 16Ω -components in the spectral signature of the blade-sleeve unsteady drag.

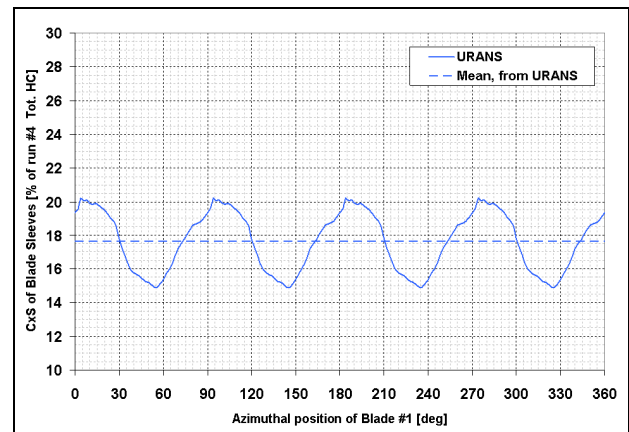


Figure 28: Cumulated unsteady drag of the four blade sleeves over the last revolution; run #4

For blade roots, cumulated unsteady drag over a rotor revolution is depicted in Figure 29. It exhibits a maximum when one blade is located in the “advancing” range of azimuth [90° ; 120°]. Variations of the cumulated drag of the blade roots over a revolution remain limited, as unsteadiness amplitudes represent less than 1% of total helicopter drag. The drag analysis of each blade separately indicates that the advancing blade root is the major contributor to the direct drag generation of the 4 blade roots. Indeed, the retreating blade root is located in

the reverse-flow circle, so that zero-or-negative drag is commonly generated in this case, while front-and-aft blade roots generate only moderate levels of pressure drag.

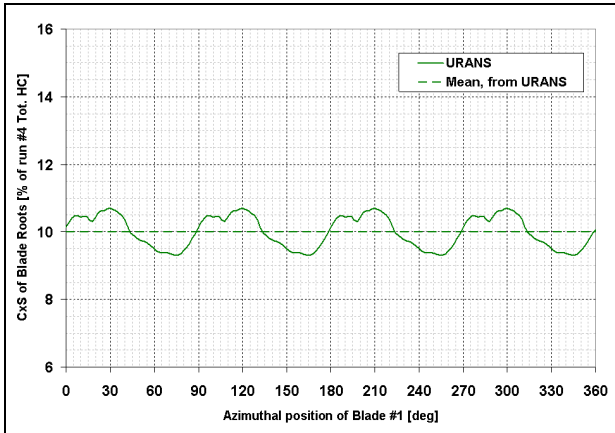


Figure 29: Cumulated unsteady drag of the four blade roots over the last revolution; run #4

3.2.2.2. Non-rotating parts

Unsteady drag of total fuselage (fuselage + pylon fairing + tail-fin + shroud) shows large variations with respect to the azimuthal position of the rotor, as illustrated by Figure 30. Rotor-head induced interaction effects over the fuselage have been included. Local maxima of fuselage drag are observed when blade #1 is azimuthally located around 120° to 150° (advancing blade region) and around 300° (retreating blade region), i.e. when blade #3 is now advancing. Minimum drag levels are observed when blades #1 and #3 are in front-or-back position. Nevertheless, maxima amplitudes seem also to be modulated by low-frequency variations.

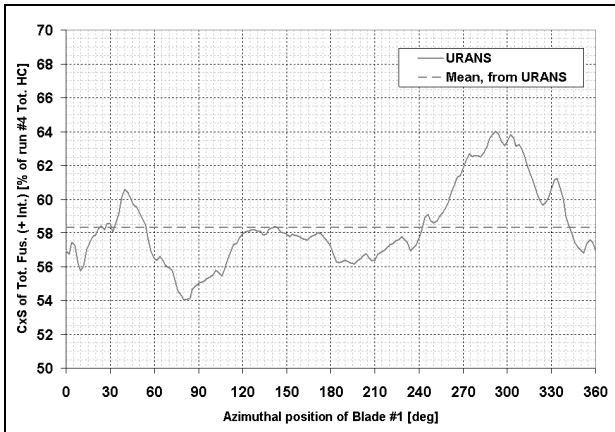


Figure 30: Unsteady drag of Total Fuselage, including interactions with Rotor head, over a revolution; run #4

Spectrum analysis shows indeed that the total-fuselage drag appears to be significantly dominated by 1 Ω - and 2 Ω -components, and not by the blade-passage frequency 4 Ω , which is fairly surprising. Several secondary peaks in the total fuselage drag spectrum have been highlighted by the analysis. Those peaks are located in frequency around 4 Ω , 10 Ω , 14 Ω and 16 Ω . The 2 Ω -peak has been revealed to be 1.2 times higher than the 1 Ω -peak, and roughly six times higher than the 4 Ω -one.

Further studies have been performed to highlight at which locations this 2 Ω -component is generated over the complete fuselage. Thus, unsteady drag has been investigated for pylon fairing and rear parts, as shown in Figure 31. Pylon-fairing drag variations over a rotor revolution are clearly dominated by the blade-passage frequency 4 Ω . Spectrum analysis demonstrates a significant presence of a 16 Ω -peak as well. A Fourier analysis of shroud unsteady drag points out that the drag is dominated by a 2 Ω -component, together with a significant 4 Ω -component, but by four times smaller in FFT amplitudes. A 6 Ω -component is also observable, but no higher orders are present in the shroud drag spectrum. Similar conclusions may be drawn from analyzing the tail-fin unsteady-drag signal.

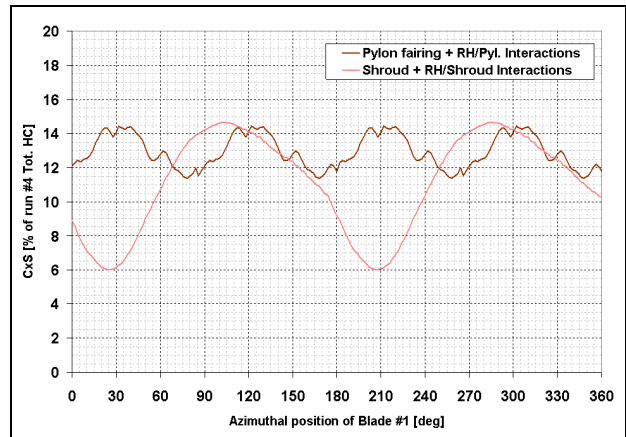


Figure 31: Unsteady drag of Pylon fairing and Shroud, including interactions with Rotor head, over the last revolution; run #4

As a consequence, it has been observed that a 4 Ω -component dominates unsteady drag spectra over fuselage parts in the vicinity of the rotor head, while rear parts drag spectra are mostly dominated by a 2 Ω -component. Some explanations may be suggested, but additional evidences would require further investigations.

One possible reason could be the presence of a vortex-pairing phenomenon during the convection of rotor-head induced wakes. Indeed, wakes generated from the rotor head usually have different origins — mast wake, sleeve wakes, root wakes, tip vortices — and exhibit different spectrum signatures accordingly. Instantaneous snapshots of vortices through iso-surfaces of Q-criterion — not available from the current simulations — should clarify the situation.

The phenomenon may also be emphasized by a higher numerical dissipation of the 4 Ω -component (and higher orders) over the 2 Ω -component throughout wake convection to rear parts. This is due to the use of low-order numerical methods on the one hand, and by mesh stretching in background grids on the other hand. In addition, the situation is getting worse by the use of second-order interpolation schemes for Chimera, because they are well known to act as low-pass filters [8].

4. CONCLUSIONS

In this paper, direct-and-indirect drag assessments have been numerically achieved for the medium-weight

helicopter Eurocopter Dauphin AS365 N3. The baseline shapes of all the rotor-hub subcomponents and fuselage have been simplified to match simplified models usually tested during wind-tunnel test campaigns, as well as to reduce costs for the meshing procedure, without altering the general trends in drag contributions. Both steady-and-unsteady simulations rely on a two-level Chimera assembly.

Steady-and-unsteady simulations indicate that significant aerodynamic gains could possibly be obtained by redesigning principally the blade sleeves, shaft (hub, mast and beanie) and blade roots, which have been revealed to be major contributors to direct drag generations. RANS simulations demonstrate that they represent respectively roughly 15%, 12% and 10% of the total helicopter drag. The influence of the azimuthal position of the rotor head has also been assessed for steady-state simulations, through the investigations of two different azimuthal positions, namely 0° and 45° with respect to the freestream direction. It reveals that the relative drag breakdown is only slightly modified by the azimuthal displacement of the rotor head, except for the contributions of two subcomponents. Blade-root direct drag increases by roughly 3% of the total helicopter and indirect drag over pylon fairing decreases by 2% when the rotor head is located at 45° .

The progressive complexification of the rotor head within the framework of RANS simulations-based investigations has made it possible to quantify each subcomponent's contribution for indirect drag. Indirect drag — which comes from wake interactions with the fuselage — is mostly generated by the blade sleeves and the blade roots by 4.5% for both components. Locations of indirect drag generation over the fuselage have been identified as well. This interaction drag is principally generated at the aft engine cowlings, at the tail-fin and at shroud. Negative interaction drag is generated at the pylon-fairing top flat surface, which seems to be a consequence of a masking effect from the aft blade.

Steady-state computations have also been revealed to be rather capable of capturing each subcomponent's relative mean-drag contributions obtained from more demanding URANS simulations with acceptable fidelity, even though the overall helicopter drag has been underestimated by 16.7%. If absolute drag levels are required, unsteady simulations seem to be mandatory, as well as for further investigations dedicated to wakes and their impact on rear fuselage parts (e.g. tail-shake).

Additional investigations could be carried out concerning the dominating 2Ω -component in the drag spectra of fuselage rear parts, in order to clarify its exact origin. The two suspected origin being vortex pairing during convection of rotor-head wake to fuselage rear parts, or numerical dissipation from low-order methods. It would also be worth investigating how the different interactional drag contributions are numerically affected by the use of other unsteady strategies such as Large Eddy Simulation, which would result in richer frequency-content of captured wakes, but also higher computational costs.

ACKNOWLEDGEMENTS

The authors wish to thank the European Clean Sky JTI Green RotorCraft Programme for supporting the research activities presented in this paper.

COPYRIGHT STATEMENTS

The authors confirm that they, and/or their company or organization, hold copyright on all of the original material included in this paper. The authors also confirm that they have obtained permission, from the copyright holder of any third party material included in this paper, to publish it as part of their paper. The authors confirm that they give permission, or have obtained permission from the copyright holder of this paper, for the publication and distribution of this paper as part of the ERF2013 proceedings or as individual offprints from the proceedings and for inclusion in a freely accessible web-based repository.

SYMBOLS

C_p	Coefficient of pressure	[-]
C_{PD}	Pressure-drag coefficient	[-]
C_{SFD}	Skin-friction drag coefficient	[-]
C_{TD}	Total drag coefficient	[-]
C_{xS}	Total drag-surface	[m ²]
e_x, e_y, e_z	Streamwise, spanwise and vertical components of the unit aerodynamic frame	[-]
\mathbf{F}_{sk}	Local friction vector at skin	[Pa]
\mathbf{n}	Local unit outward-pointing vector normal to wall	[-]
N_r	Rotor-head rotational speed	[rpm]
W	Vertical component of the velocity vector	[m/s]
p_∞	Reference (far-field) pressure	[Pa]
T_∞	Reference (far-field) temperature	[K]
U_∞	Freestream velocity	[m/s]
α	Pitch angle	[deg]
β	Sideslip angle	[deg]
Δ_{TD}	Total drag density difference	[-]
ρ_∞	Reference air density	[kg/m ³]
$\boldsymbol{\tau}_{wall}$	Viscous stress tensor at the wall	[Pa]
ψ	Blade #1 azimuth angle	[deg]
Ω	Rotor-head frequency	[Hz]

REFERENCES

- [1] Borie, S., Mosca, J., Sudre, L., Benoit, C. & Péron, S. "Influence of rotor wakes on helicopter aerodynamic behaviour", 35th European Rotorcraft Forum, Hamburg, Germany (2009).
- [2] Kneisch, T., Krauss, R., D'Alascio, A., & Schimke, D., "Optimised rotor-head design for an economic helicopter", 37th European Rotorcraft Forum, Gallarate, Italy (2011).
- [3] Grawunder, M, Ress, R., Breitsamter, C. & Adams, N.A., "Flow characteristics of a helicopter fuselage configuration including a rotating rotor head", 28th International Congress of the Aeronautical Sciences, Brisbane, Australia (2012).

- [4] Leishman, J.G. "Principles of Helicopter Aerodynamics", 2nd edition, Cambridge Aerospace Series (2006).
- [5] Menter, F.R., "Two-Equation Eddy-Viscosity Turbulence Models for Engineering Applications", AIAA Journal, Vol. 32, No. 8, pp. 1598-1605 (1994).
- [6] Benek, J.A., Steger, J.L. & Dougherty, F.C. "A flexible grid embedding technique with applications to the Euler equations", AIAA paper 83-1944 (1983).
- [7] Benek, J.A., Steger, J.L., Dougherty, F.C. & Buning, P.G. "Chimera: a grid-embedding technique", AECD Technical Report 85-64 (1986).
- [8] Desvigne, D., Marsden, O., Bogey, C. & Bailly, C. "Development of noncentered wavenumber-based optimized interpolation scheme with amplification control for overlapping grids", SIAM J. Sci. Comput. Vol. 32, pp. 2074-2098 (2010).
- [9] ONERA DSNA, "User's reference manual for the elsA software v3.4", (2012).
- [10] Meakin R.T., "Object X-Rays for cutting holes in Composite Overset Structured Grids", 15th AIAA Computational Fluid Dynamics Conference (2001).
- [11] Benoît, B., Dequin, A.M., Kampa, K., von Grünhagen, W., Basset, P.M. & Gimonet, B., "HOST, a General Helicopter Simulation Tool for Germany and France", 56th Annual Forum of the American Helicopter Society (2000).